Supporting information

Locking the Spin States of Anionic $Fe(L)_2$ Units in Coordination Polymers through Alkali Metal Ions Incorporation

Jing-Yao Zhou,[a,b,c] Hong-Dong Zhang,[a,b,c] Fan Yin,[b,c] Zheng-Zhong Zhu,[b,c] Li-peng Zhou,[b,c] Chong-Bin Tian*[a,b,c] and Qing-Fu Sun*[a,b,c]

[a] College of Chemistry, Fuzhou University, Fuzhou 350108, People's Republic of China.

[b] State Key Laboratory of Structural Chemistry, Fujian Institute of Research on the Structure of Matter, Chinese Academy of Sciences, Fuzhou 350002, China

[c] Fujian College, University of Chinese Academy of Sciences, Fuzhou 350002, People's Republic of China.

Email: tianchongbin@fjirsm.ac.cn, qfsun@fjirsm.ac.cn.

Contents

1. Experimental procedures

1.1 General

Unless otherwise stated, all chemicals and solvents were purchased from commercial companies and used directly. Deuterated solvents were purchased from Admas, J&K scientific and Sigma-Aldrich. ^{1}H-NMR spectra were determined on JEOL ECZ600S (600 MHz) spectrometer, and the variable temperature (VT) H-NMR spectra were measured on JEOL ECZ600S (600 MHz) spectrometer. Besides, ^{1}H-NMR chemical shifts were measured with respect to residual signals of the deuterated solvents used. ESI mass spectrometry (MS) experiments were performed on a Waters Synapt HDMS G2-Si quadrupole/time -of-flight (Q/TOF) tandem mass spectrometer. This instrument contains a triwave device between the Q and TOF analyzers, consisting of three collision cells in the order trap cell, ion mobility cell, and transfer cell. Trap and transfer cells are pressurized with Ar, and the ion mobility cell is pressurized with N_2 flowing in a direction opposite to that of the entering ions. FT-IR spectra were recorded on a Bruker VERTEX70 spectrometer equipped with an attenuated total reflection (ATR) accessory. Additionally, elemental analyses of C, H, and N were measured using a Vario EL III elemental analyzer. Thermogravimetric analyses were performed using a GA/NETZSCH STA449C instrument heated from 20−800 °C (heating rate of 10 °C min^{-1}, nitrogen stream). The X-ray powder diffraction (XPRD) data were collected using Miniflex600 (Cu-Kα radiation: λ = 1.54056 Å) in the range of $5° < 2\theta < 50°$. Variable-temperature magnetic susceptibility data were collected with a Quantum Design MPMS XL superconducting quantum interference device (SQUID) magnetometer under an applied magnetic field of 1 kOe in sweep mode with a scan speed of 2 K min^{-1}. UV-Vis spectra are recorded on UV-2700 UV-Visible spectrophotometer from SHIMADZU. Diamagnetic corrections were made using Pascal's constants. Otherwise, TGA, elemental analyses, and variable-temperature magnetic susceptibility were performed by Crystal powder.

Caution! The pyridine-2,6-bi-tetrazolate-based ligands and their derivatives are potentially explosive, hence extreme care should be taken with small quantity in using and handing with them.[1]

1.2 Syntheses and Characterization

Synthesis of self-assembled complex of H_2L:

The ligand H_2L (Pyridine-2,6-bi-tetrazolate) was synthesized by cycloaddition of sodium azide with the pyridine-2,6-dicarbonitrile in anhydrous dimethylformamide (more details see Ref S1).[1, 2]

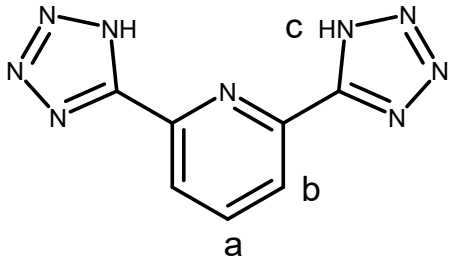

Figure S1. Structure of the **H_2L**.

Synthesis of self-assembled complex 1: Dissolve H_2L (43.00 mg, 0.2 mmol, 1.0 equivalent) in methanol (10 mL), add lithium hydroxide (LiOH) (9.58 mg, 0.4 mmol, 2.0 equivalents), and stir at room temperature for 15 minutes until the solution becomes clear. Subsequently, add $Fe(OTf)_2$ (35.398 mg, 0.1 mmol, 0.5 equivalents) to the solution. Stir the reaction at 50 °C for 30 minutes, during which the solution gradually turns reddish-orange. Once the solution becomes clear, add a large amount of diethyl ether to precipitate the red precipitate. Collect the precipitate by centrifugation. The precipitate was redissolved in a mixture of water and methanol (v/v = 2/1). The resulting solution was allowed to stand and evaporate to dryness under air for two weeks, yielding a deep red single crystal of product **1**. The crystal was collected, washed with diethyl ether, and dried to afford a deep red crystalline powder of product 1 (56.97 mg, 89% yield based on Fe). Anal. calcd. (%) for **1** $C_{14}H_{22}FeLi_2N_{18}O_8$ (640.153): C 26.24, N 39.36, H 3.43. Found: C 26.09, N 38.94, H 3.35. ^{1}H NMR (600 MHz, d_6-DMSO) δ 27.31 (s, 2H), 14.20 (s, 1H).

Synthesis of self-assembled complex 2: The synthesis process was similar to **1** except that NaOH (16.0 mg, 0.4 mmol) was used instead of LiOH. The preparation of single crystals and powder were also similar to **1**. After volatilization of the aqueous phase, 40.71 mg of yellow crystal was obtained (64% yield, based on Fe). Anal. calcd. (%) for **2** $C_{14}H_{18}FeN_{18}Na_2O_6$ (636.08): C 26.41, N 39.62, H 2.83. Found: C 26.96, N 39.92, H 2.76. ^{1}H NMR (600 MHz, d_6-DMSO) δ 25.65 (s, 2H), 13.75 (s, 1H).

Synthesis of self-assembled complex 3: The synthesis process was similar to **1** except

that KOH (22.44 mg, 0.4 mmol) was used instead of LiOH. The preparation of single crystals and powder were also similar to **1**. A trace amount of yellow crystals were obtained through water-phase evaporation crystallization.^{1}H NMR (600 MHz, d_6-DMSO) δ 28.40 (s, 2H), 14.53 (s, 1H).

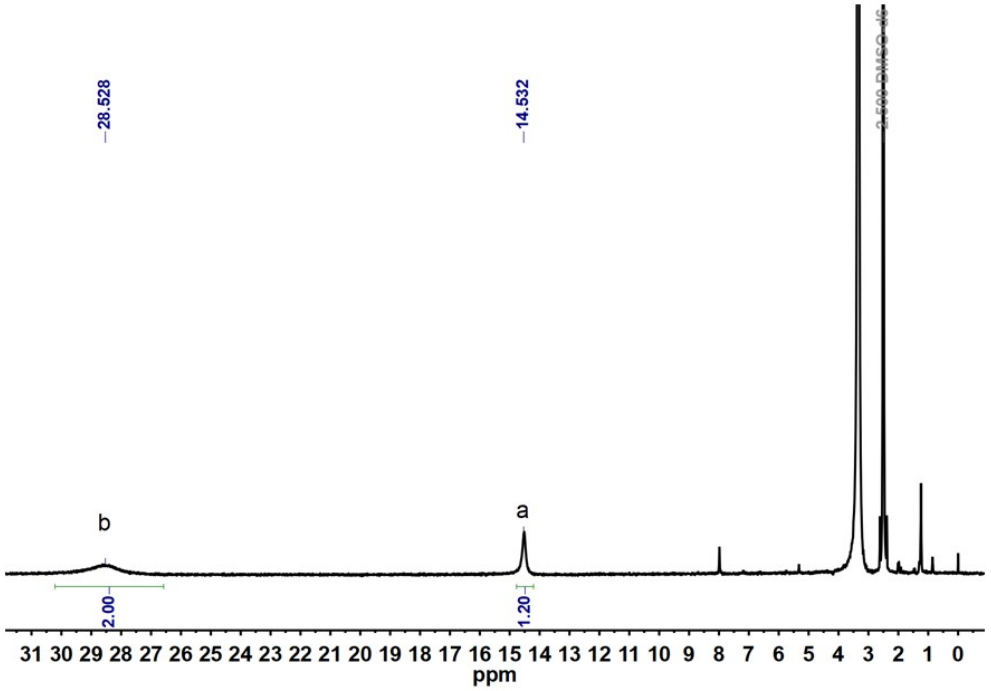

Figure S2. ^{1}H-NMR spectrum of **1** (600 MHz, d_6-DMSO, 298 K).

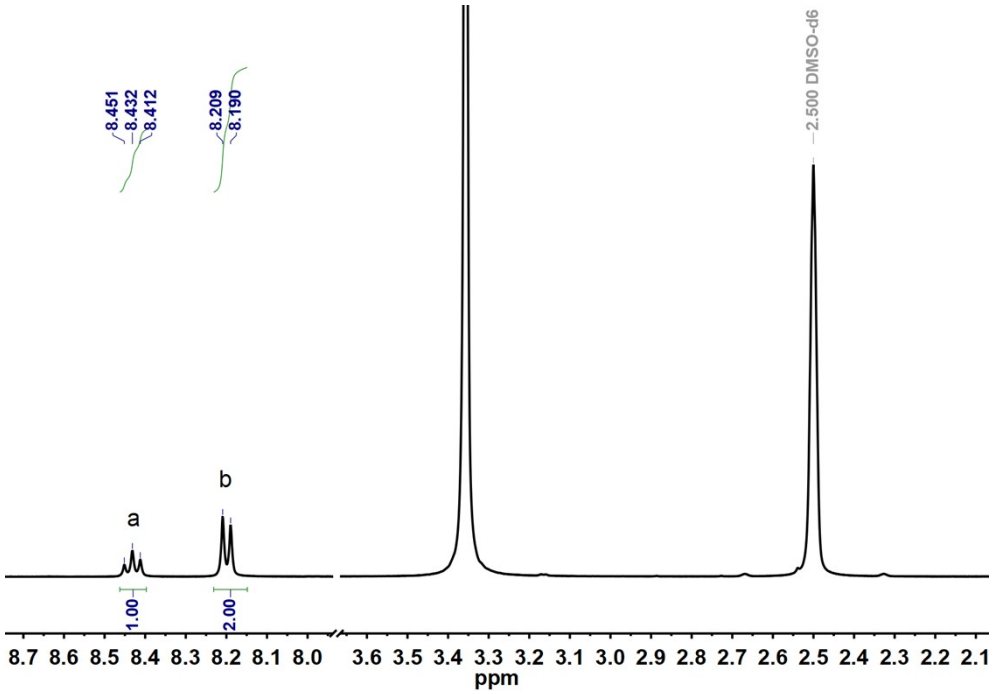

Figure S3. ^{1}H-NMR spectrum of Zn analogue of compound **1** (600 MHz, d_6-DMSO, 298 K).

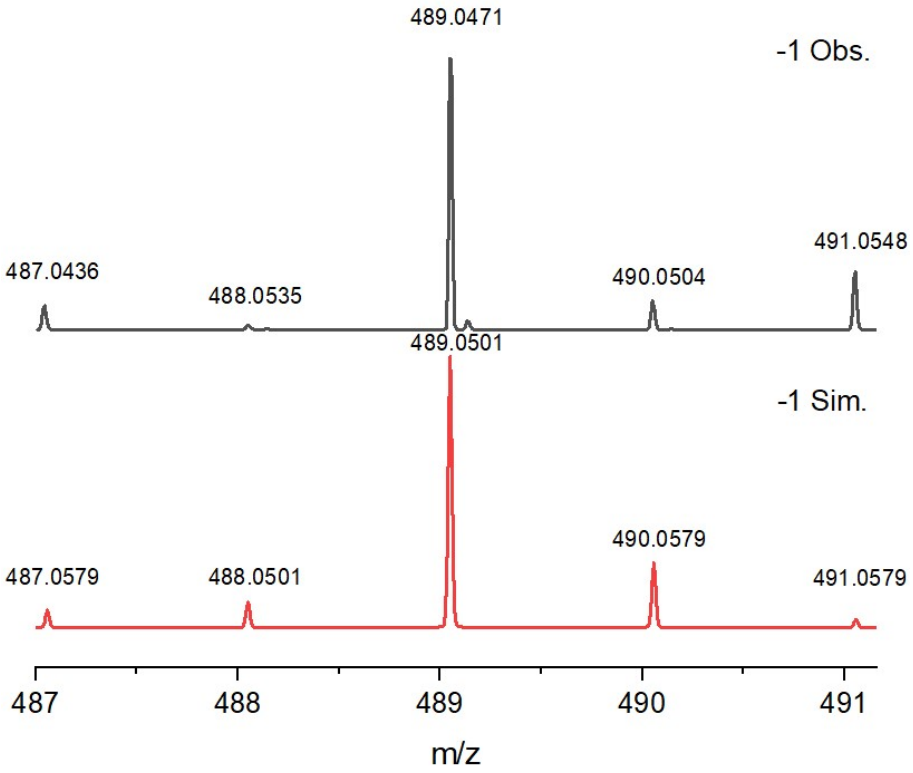

Figure S4. ESI-TOF-MS spectrum of compound **1**, showing the observed and simulated isotope distribution patterns for the −1 peak.

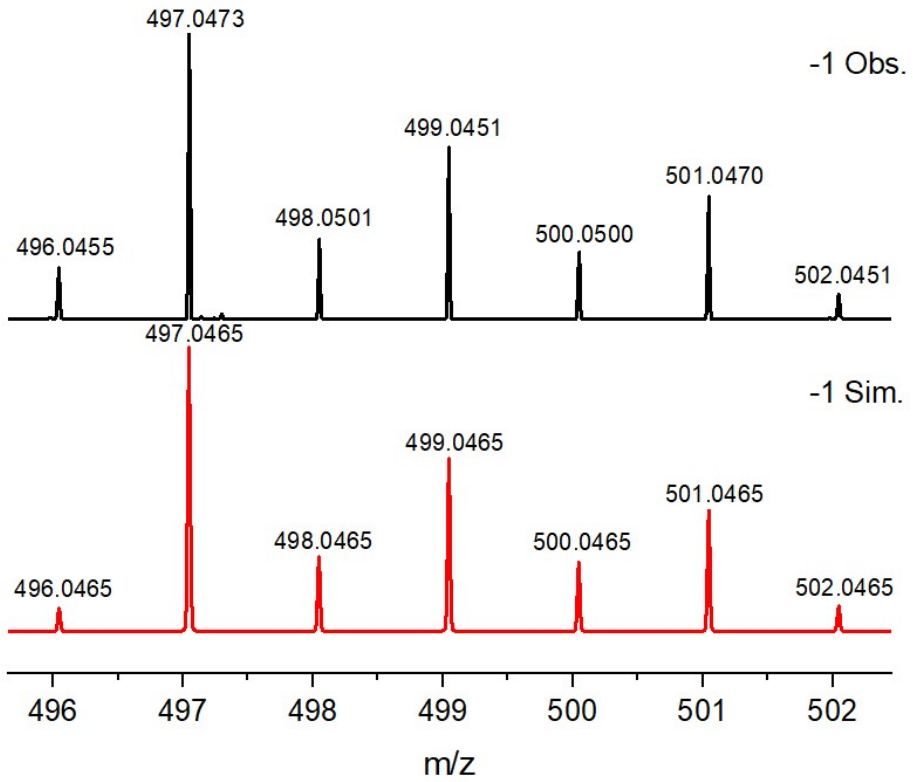

Figure S5. ESI-TOF-MS spectrum of Zn analogue of compound **1**, showing the observed and simulated isotope distribution patterns for the −1 peak.

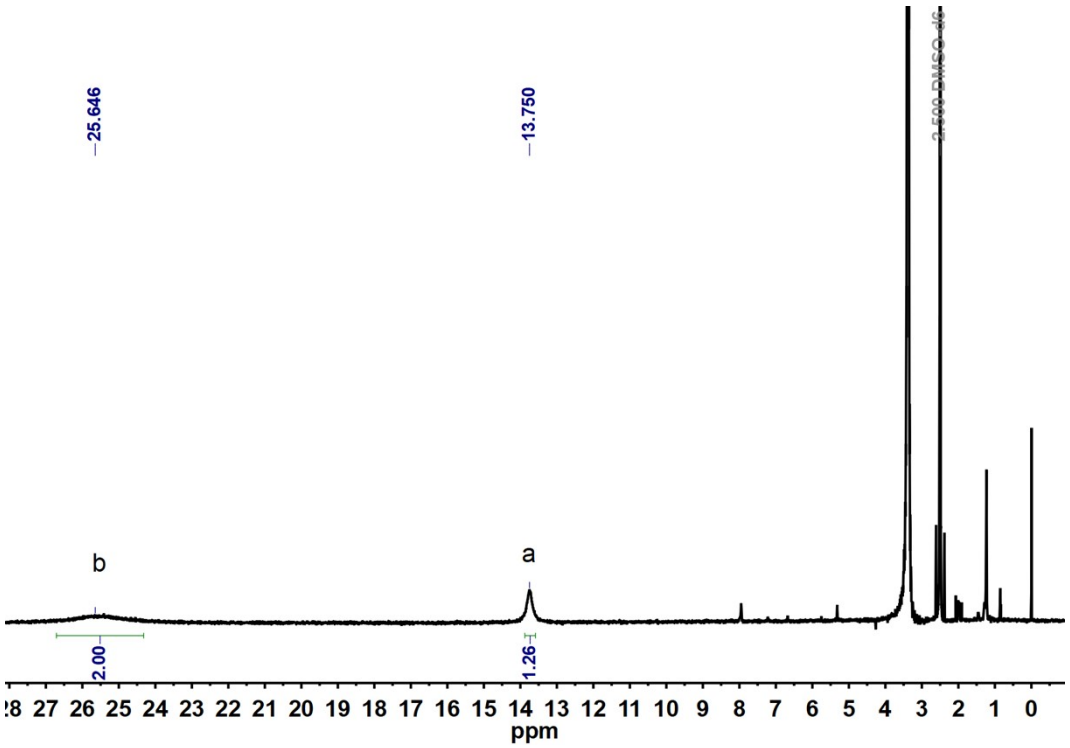

Figure S6. ^{1}H-NMR spectrum of **2** (600 MHz, d_6-DMSO, 298 K).

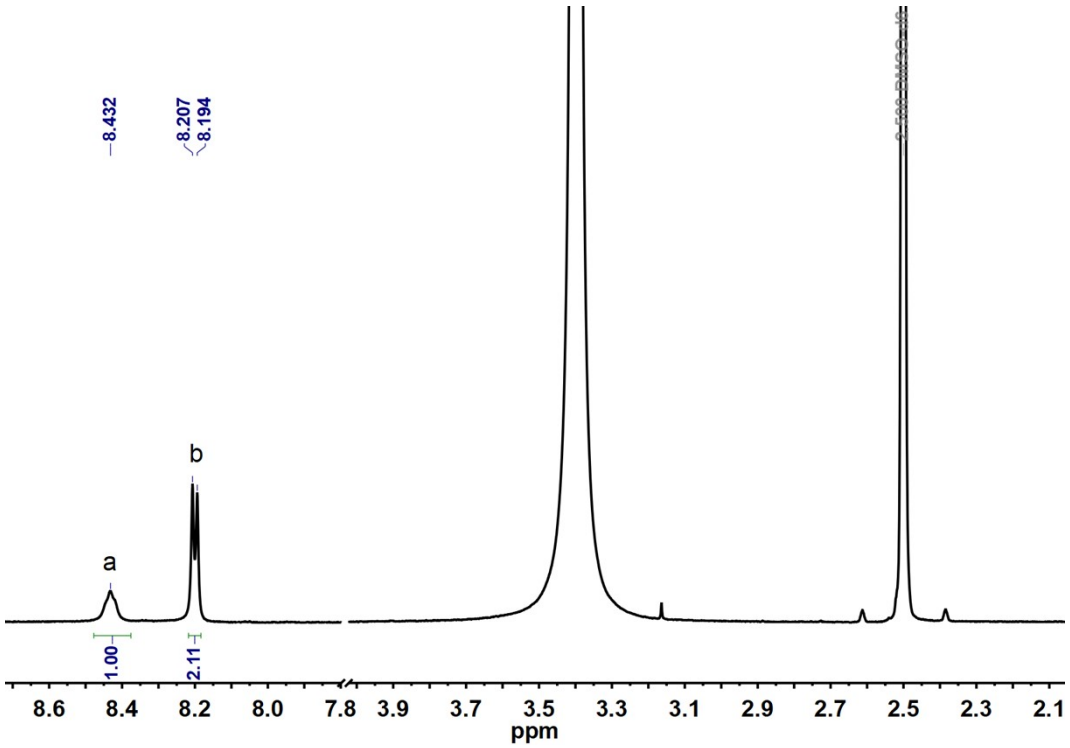

Figure S7. ^{1}H-NMR spectrum of Zn analogue of compound **2** (600 MHz, d_6-DMSO, 298 K).

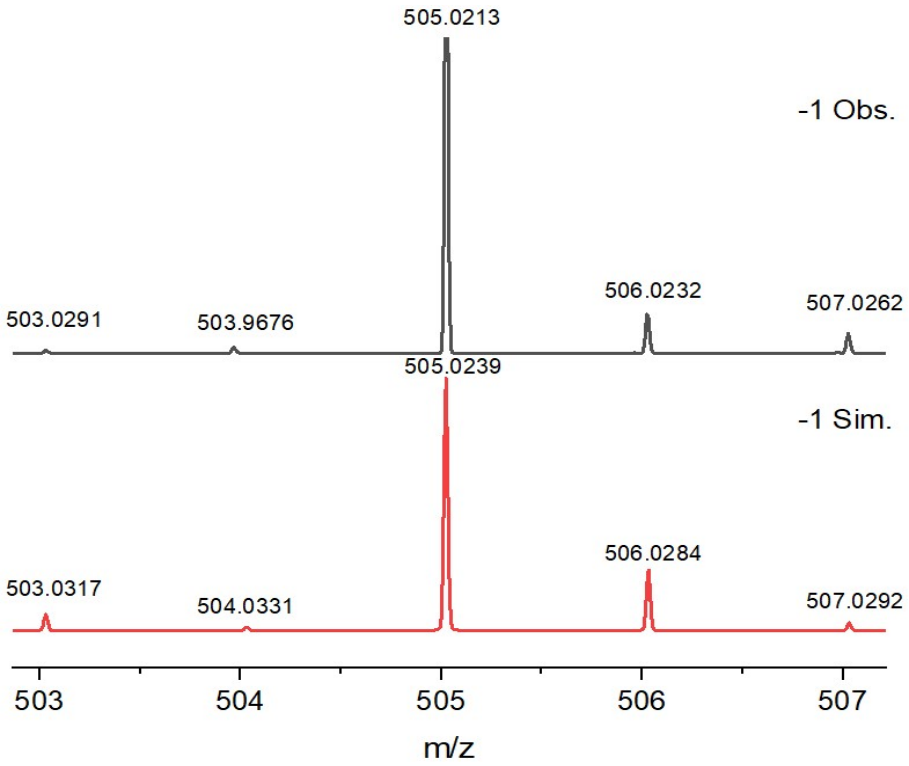

Figure S8. ESI-TOF-MS spectrum of compound **2**, showing the observed and simulated isotope distribution patterns for the −1 peak.

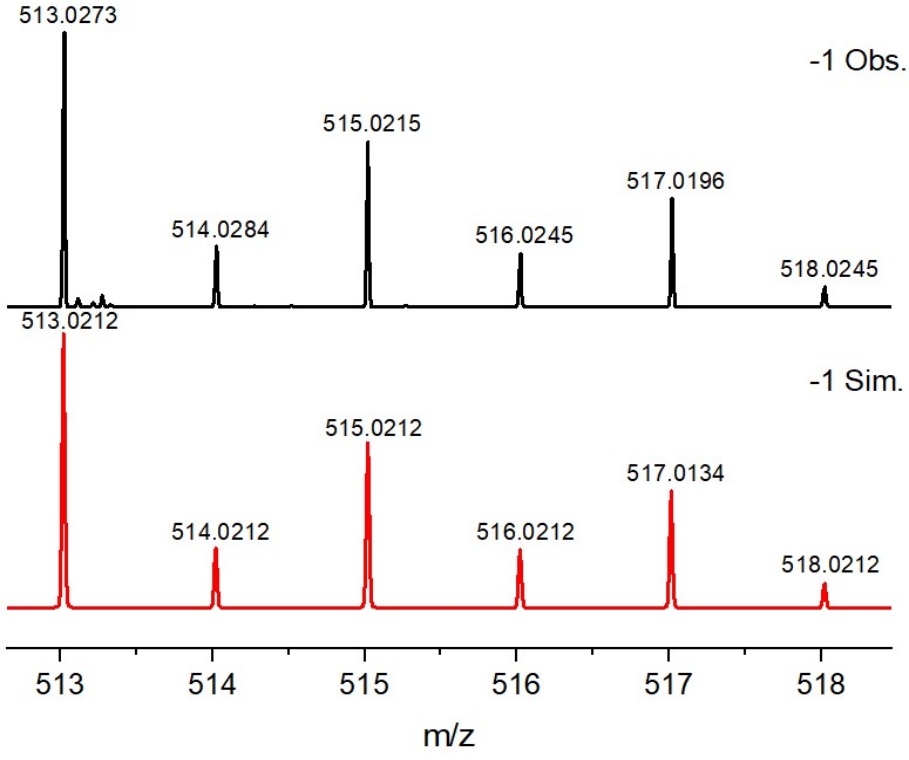

Figure S9. ESI-TOF-MS spectrum of Zn analogue of compound **2**, showing the observed and simulated isotope distribution patterns for the −1 peak.

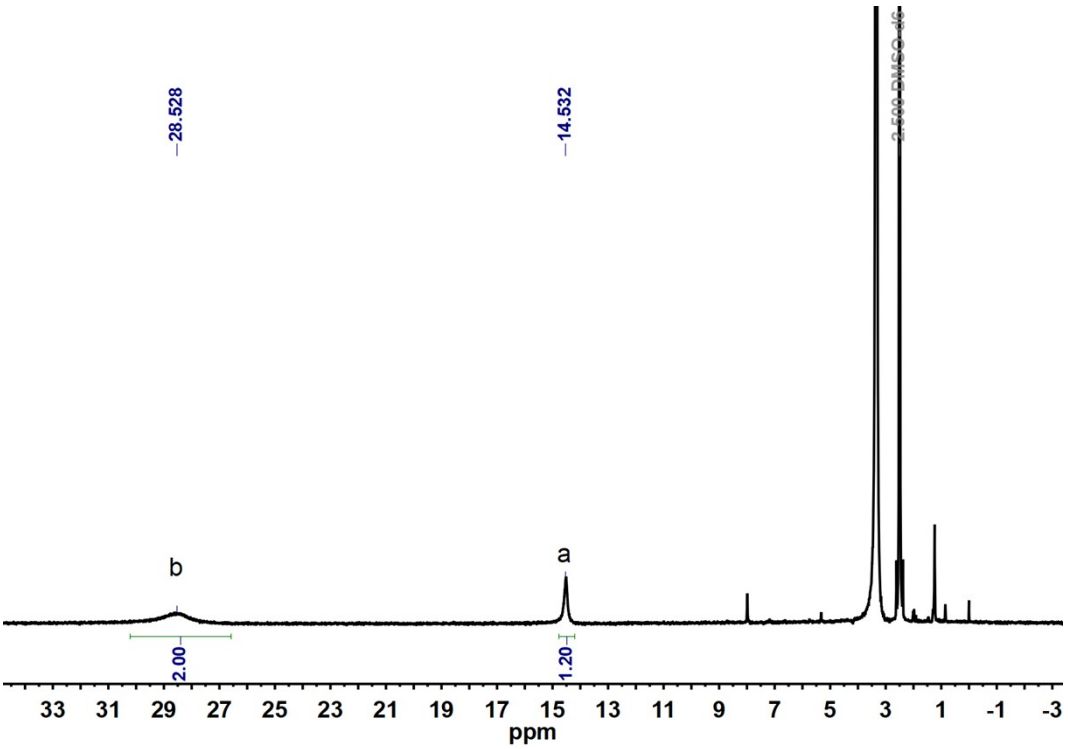

Figure S10. ^{1}H-NMR spectrum of **3** (600 MHz, d_6-DMSO, 298 K).

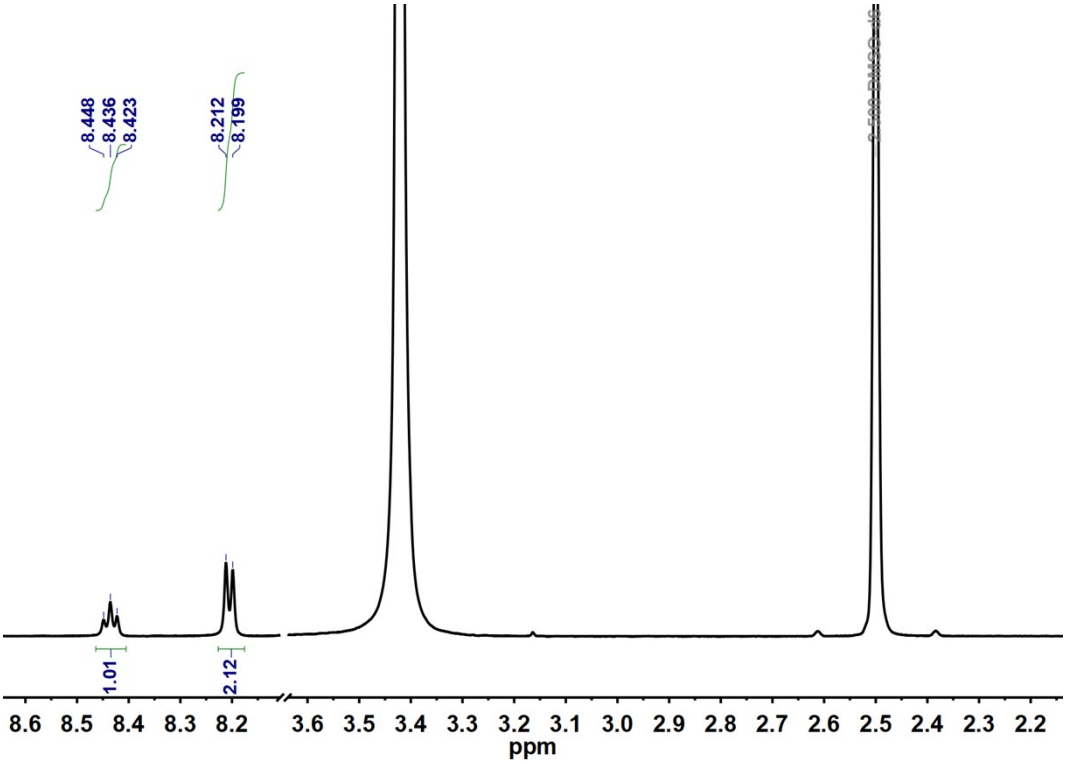

Figure S11. ^{1}H-NMR spectrum of Zn analogue of compound **3** (600 MHz, d_6-DMSO, 298 K).

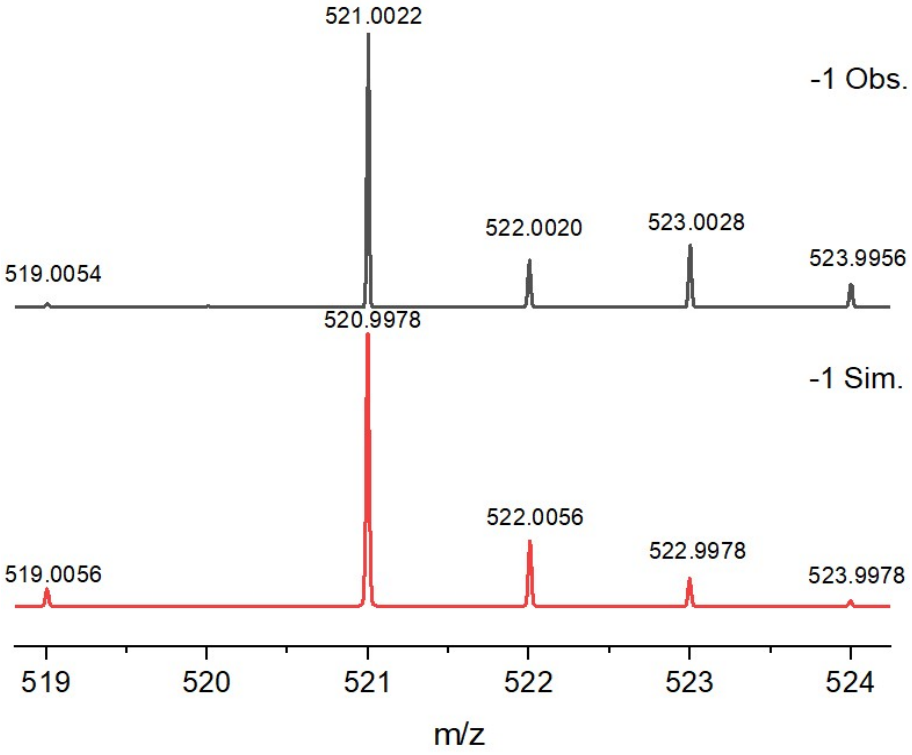

Figure S12. ESI-TOF-MS spectrum of compound **3**, showing the observed and simulated isotope distribution patterns for the −1 peak.

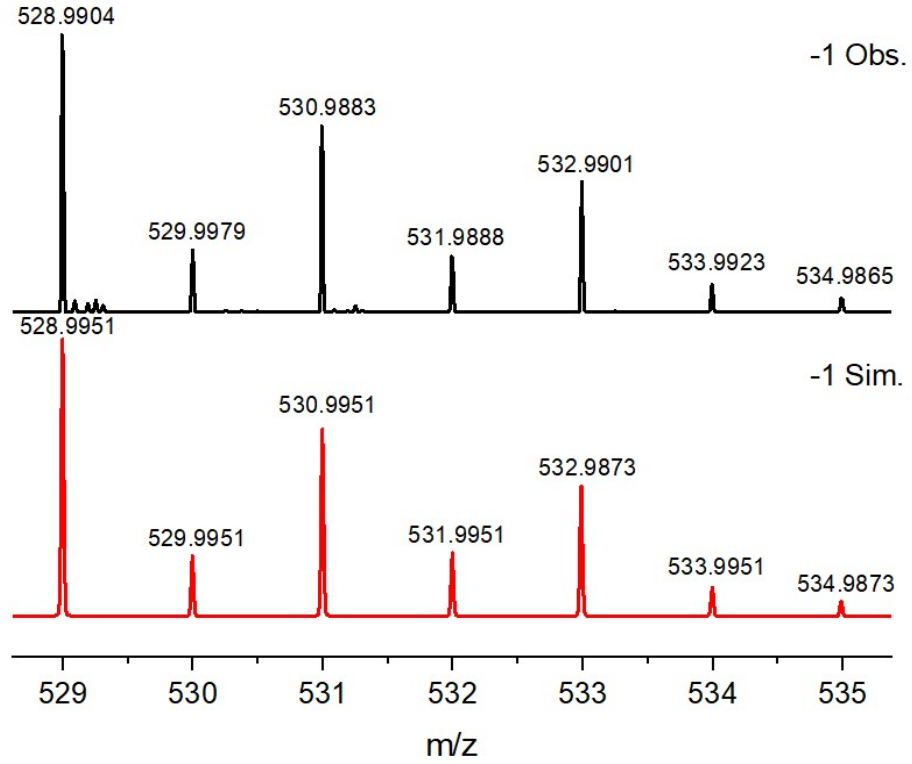

Figure S13. ESI-TOF-MS spectrum of Zn analogue of compound **3**, showing the observed and simulated isotope distribution patterns for the −1 peak.

2. UV−Vis Spectroscopy

The UV–Vis spectra of complexes **1**−**3** are very similar (Figure S14), which show strong absorption in the 270–310 nm ranges, due to the π → π* and n → π* transitions on the aromatic ligands. In addition, the band at ca. 500 nm corresponds to charge transfer (CT) bands.

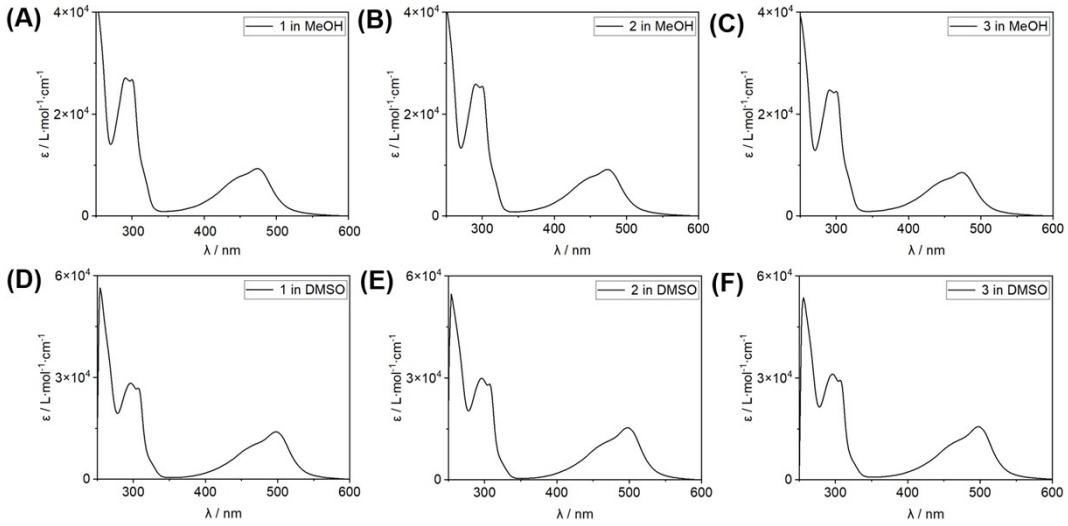

Figure S14. UV/Vis absorption spectra of **1**−**3** (c = 2.00 × 10^{-5} M in methanol and DMSO at 298 K).

3. ATR-FTIR

FT-IR spectra were recorded on a Bruker VERTEX70 spectrometer equipped with an attenuated total reflection (ATR) accessory. The infrared spectra of compounds **1**−**3** show a broad, strong band at 3600−3200 cm^{-1} from O−H stretches of water molecules. Features in the 1680−1550 cm^{-1} region are due to C=N stretches of the tetrazolyl rings, while bands in the 600−400 cm^{-1} range are characteristic of Fe–N bonds, verifying successful metal-ligand coordination.

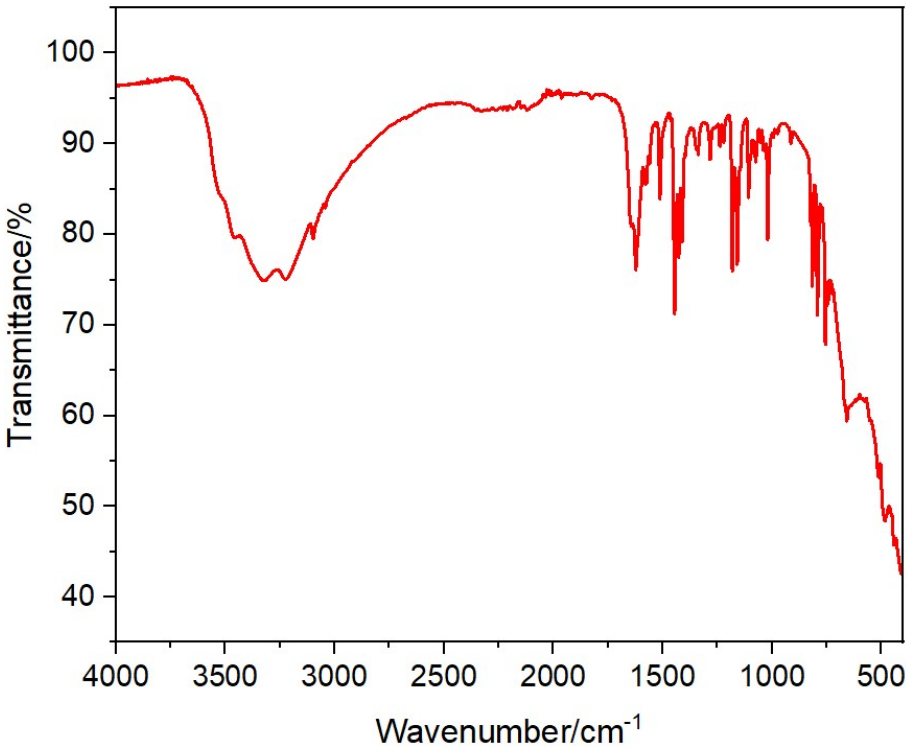

Figure S15. IR spectra of **1**.

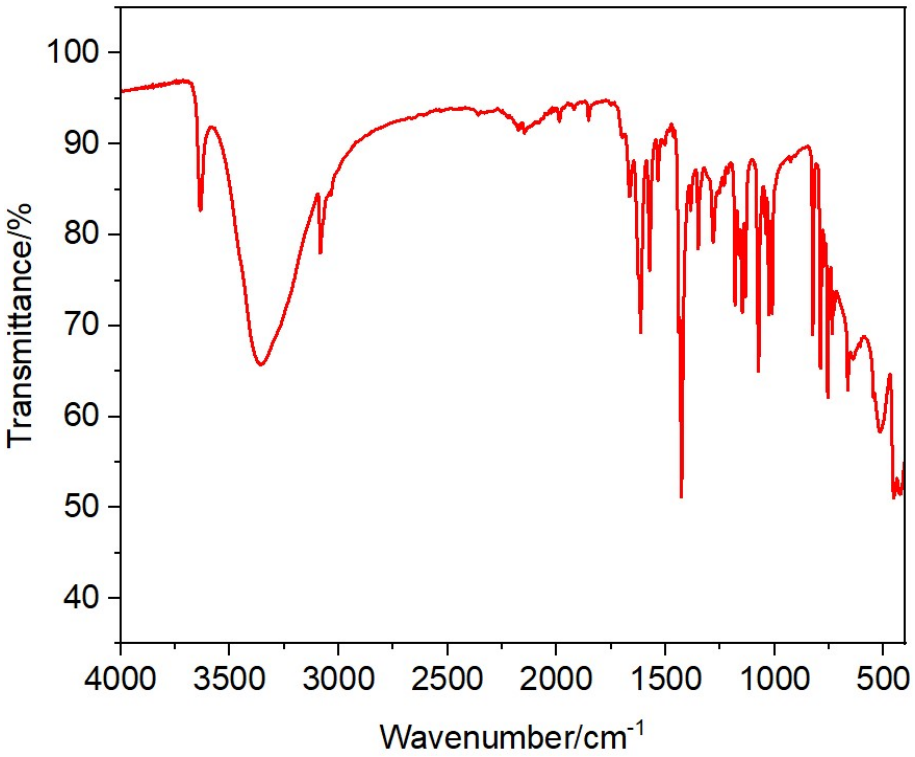

Figure S16. IR spectra of **2**.

4. Single crystal X-ray diffraction studies

The single crystals X-ray diffraction was carried out on micro-focus metaljet diffractometer using Ga Kα radiation (λ = 1.3405 Å). And data reduction was performed with the CrysAlisPro package[3], at last analytical absorption correction was performed. All structures were solved by direct methods and refined by full-matrix least-squares on F^2 with anisotropic displacement using the Olex2 software package[4]. The crystallographic data and other relevant information for Compounds **1**−**3** are summarized below.

Table S1. Crystallographic data and structure refinement parameters for complexes **1–3** at different temperatures.

	1 (293 K)	**2 (100 K)**	**3 (240 K)**
Empirical	$C_{14}H_{22}FeLi_2N_{18}O_8$	$C_{14}H_{18}FeN_{18}Na_2O_6$	$C_{16}H_{14}FeK_2N_{18}O_2$
Fw	640.22	636.29	624.50
Cryst syst	Orthorhombic	Orthorhombic	Orthorhombic
Space group	Cccm	$Pca2_1$	Pbcn
a/Å	13.9830(5)	13.6942(4)	13.5376(6)
b/Å	21.1145(11)	7.7375(2)	8.0985(4)
c/Å	8.9586(4)	23.4883(8)	21.7556(10)
α/°	90	90	90
β/°	90	90	90
γ/°	90	90	90
V/Å^3	2645.0(2)	2488.79(13)	2385.16(19)
Z	4	4	4
ρ_{calc}/g cm^{-3}	1.608	1.698	1.739
μ/mm^{-1}	5.267	0.714	5.943
F(000)	1312.0	1296.0	1264.0
Parameters	107	376	182
R_1[a],wR_2[b][I>2σ(I)]	0.0373/0.1006	0.0324/0.0815	0.0575/0.1244
R_1[a],wR_2[b][all data]	0.0401/0.1022	0.0390/0.0855	0.0747/0.1319
Goodness-of-fit	1.076	1.083	1.088

[a]$R_1=\Sigma||F_0|-|F_c||/\Sigma|F_0|$, [b]$wR_2=[\Sigma w(F_0^2-F_c^2)^2/\Sigma w\,(F_0^2)^2]^{0.5}$.

Table S2. Selected Bond Lengths (Å) and Angles (º) for **1**.

Fe1-N2^{i}	1.9745(15)	Fe1-N2^{iii}	1.9746(15)
Fe1-N2	1.9745(15)	Fe1-N1	1.982(2)
Fe1-N2^{ii}	1.9745(15)	Fe1-N1^{iii}	1.982(2)
N2^{i}-Fe1-N2^{ii}	90.23(9)	N2^{ii}-Fe1-N2^{iii}	159.59(9)
N2^{iii}-Fe1-N2	90.23(9)	N2^{i}-Fe1-N2^{iii}	93.37(9)
N2^{i}-Fe1-N2	159.59(9)	N2^{ii}-Fe1-N2	93.37(9)
N1^{ii}-Fe1-N2	100.21(4)	N1^{ii}-Fe1-N2^{iii}	79.79(4)
N1-Fe1-N2^{i}	79.79(4)	N1-Fe1-N2	79.79(4)
N1^{ii}-Fe1-N2^{ii}	79.79(4)	N1-Fe1-N2^{ii}	100.21(4)
N1^{ii}-Fe1-N2^{i}	100.21(4)	N1-Fe1-N2^{iii}	100.21(4)
N1-Fe1-N1^{ii}	180.0		

Symmetry codes: (i) +X,1/2-Y,1/2-Z; (ii) 1-X,1/2-Y,+Z; (iii) 1-X,+Y,1/2-Z.

Table S3. Selected Bond Lengths (Å) and Angles (º) for **2**.

Fe1-N14	2.214(3)	Fe1-N18	2.168(3)
Fe1-N5	2.207(3)	Fe1-N10	2.203(3)
Fe1-N9	2.161(3)	Fe1-N1	2.209(3)
N5-Fe1-N14	81.44(11)	N9-Fe1-N5	73.81(13)
N5-Fe1-N1	147.06(12)	N9-Fe1-N18	173.11(8)
N9-Fe1-N14	110.58(13)	N9-Fe1-N10	102.45(14)
N9-Fe1-N1	73.66(12)	N18-Fe1-N1	110.90(13)
N18-Fe1-N14	73.66(12)	N10-Fe1-N14	146.88(12)
N18-Fe1-N5	101.97(14)	N10-Fe1-N5	110.93(8)
N18-Fe1-N10	73.72(12)	N10-Fe1-N1	81.19(11)
N1-Fe1-N14	105.36(8)		

Table S4. Selected Bond Lengths (Å) and Angles (º) for **3**.

Fe1-N5	2.171(2)	Fe1-N5^{i}	2.171(2)
Fe1-N4	2.273(2)	Fe1-N4^{i}	2.273(2)
Fe1-N6^{i}	2.195(2)	Fe1-N6	2.195(2)
N5-Fe1-N5^{i}	175.39(12)	N5-Fe1-N4	104.21(8)
N5^{i}-Fe1-N4^{i}	72.91(8)	N5^{i}-Fe1-N4	104.21(8)
N5-Fe1-N4	72.91(8)	N5-Fe1-N6	109.20(9)
N5-Fe1-N6	73.87(8)	N5^{i}-Fe1-N6	109.20(9)
N5^{i}-Fe1-N6^{i}	73.87(9)	N4-Fe1-N4^{i}	105.87(12)
N6^{i}-Fe1-N4	85.93(9)	N6-Fe1-N4^{i}	85.93(9)
N6^{i}-Fe1-N4^{i}	146.54(9)	N6-Fe1-N4	146.55(9)
N6^{i}-Fe1-N4	146.55(9)		

Symmetry codes: (i) 3/2-X,+Y,1-Z.

Table S5. The H-bonds interactions in compound **1**.

Interaction	**d(D-H)/ Å**	**d(H···A)/ Å**	**d(D···A)/ Å**	**<(DHA)/°**
O2-H2^{i}···N5^{i}	0.85	2.10	2.926(2)	162.7
O2-H2^{ii}···N3^{ii}	0.85	2.16	2.984(2)	162.7
O1-H1^{ii}···O2	0.85	1.94	2.751(3)	158.9
O1-H1^{ii}···O2^{iii}	0.85	2.18	2.983(3)	156.7

Symmetry codes: (i) 3/2-X,1-Y,+Z; (ii) 1-X,1-Y,1-Z; (iii) +X,1-Y,1/2+Z.

Table S6. The H-bonds interactions in compound **2**.

Interaction	d(D-H)/ Å	d(H···A)/ Å	d(D···A)/ Å	<(DHA)/°
O5-H5^{ii}···O2	0.87	2.49	2.861(6)	106.1
O5-H5^{ii}···O1^{ii}	0.87	2.48	2.884(6)	109.1
O1-H1^{i}···N3^{iii}	0.99	1.86	2.817(5)	161.1
O1-H1^{ii}···O5^{iv}	0.99	1.95	2.884(6)	156.0
O3-H3^{i}···N16^{ii}	0.99	1.91	2.848(5)	157.7
O3-H3^{ii}···N06^{ii}	0.99	1.93	2.895(6)	163.6
O6-H6^{i}···O3^{iv}	0.87	2.42	2.895(6)	115.1
O4-H4^{i}···O6	0.99	1.93	2.880(6)	160.7

Symmetry codes: (i) 1-X,1-Y,-1/2+Z; (ii) +X,1+Y,+Z; (iii) 1-X,-Y,-1/2+Z; (iv) +X,-1+Y,+Z.

Table S7. The H-bonds interactions in compound **3**.

Interaction	d(D-H)/ Å	d(H···A)/ Å	d(D···A)/ Å	<(DHA)/°
C3-H3-N7^{i}	0.94	2.82	3.439(4)	124.7
C4-H4-N7^{i}	0.94	2.85	3.463(4)	124.1
C8-H8^{iii}-N7^{ii}	0.97	2.44	3.398(5)	170.9
O1-H1-N1^{iii}	0.85(7)	2.17(8)	2.832(4)	135(3)

Symmetry codes: (i) 1/2+X,1/2+Y,1/2-Z; (ii) +X,1-Y,1/2+Z; (iii) -1/2+X,3/2-Y,1-Z.

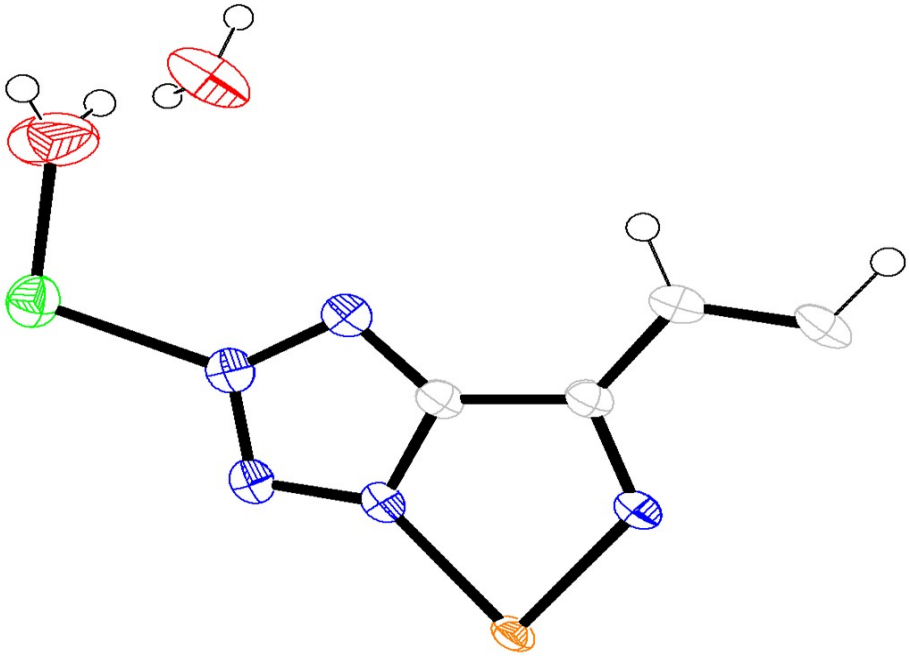

Figure S17. Ortep drawing of the asymmetric unit in the crystal structure of **1** at 50% probability.

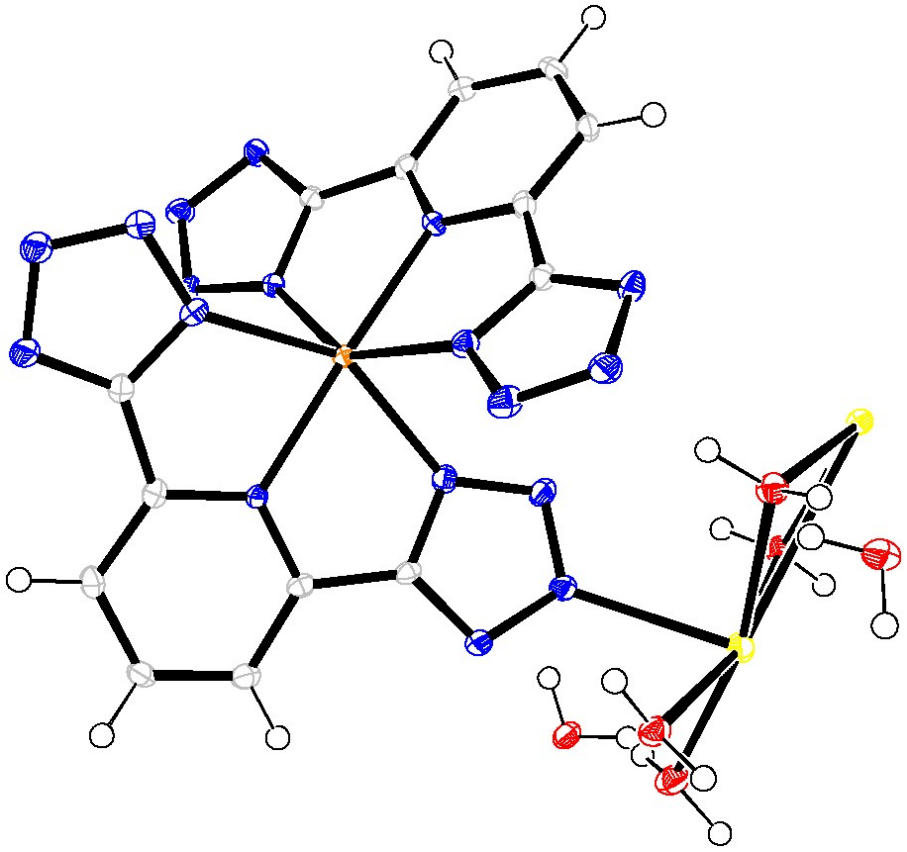

Figure S18. Ortep drawing of the asymmetric unit in the crystal structure of **2** at 50%

probability.

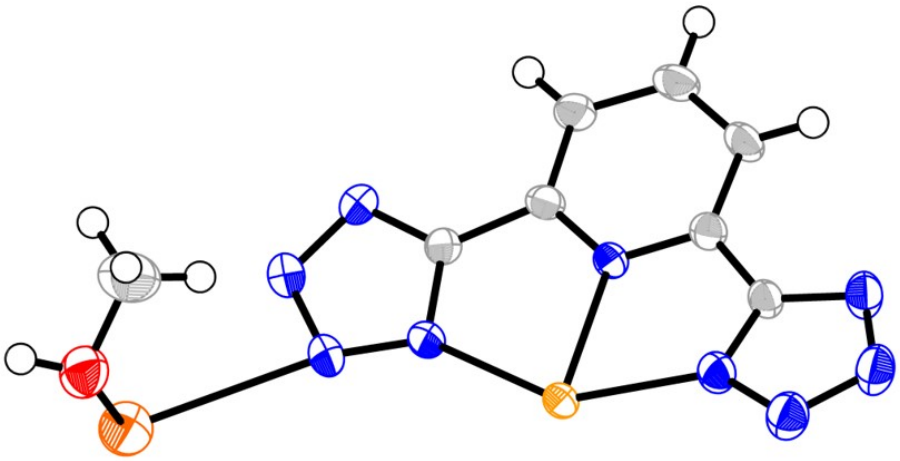

Figure S19. Ortep drawing of the asymmetric unit in the crystal structure of **3** at 50% probability.

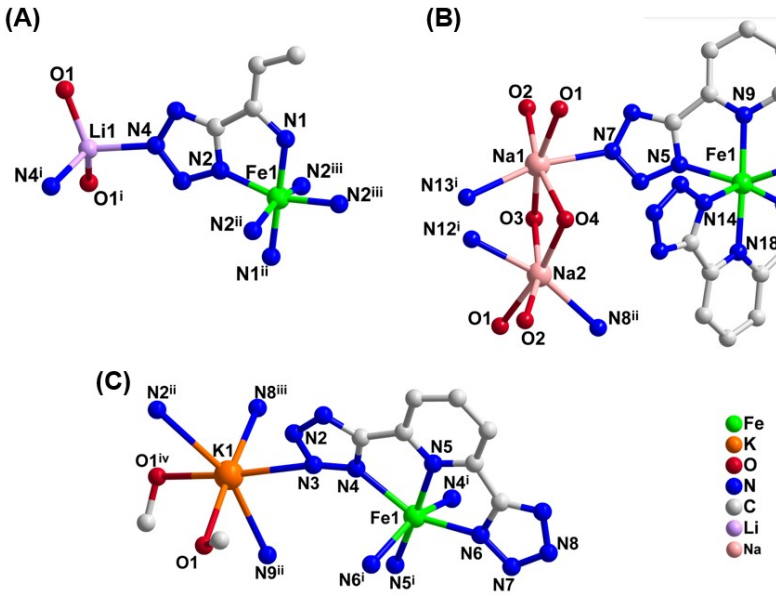

Figure S20. (A) Coordination environments of the Li^{I} and Fe^{II} ions in **1**. Symmetry codes: i = (1−X, Y, 3/2−Z); ii = (1−X, 1/2−Y, Z), iii = (X, 1/2−Y, 1/2−Z) . (B) Coordination environments of the Na^{I} and Fe^{II} ions in **2**. Symmetry code: i = (3/2-X, Y, -1/2+Z), ii = (1/2+X, 1−Y, Z). (C) Coordination environments of the K^{I} and Fe^{II} ions in **3**. Symmetry codes: i = (1−X, Y, 1/2−Z); ii = (1−X, −2−Y, 1−Z); iii = (1−X, 1+Y, 1/2−Z); iv = (1/2-X, 1/2+Y, Z).

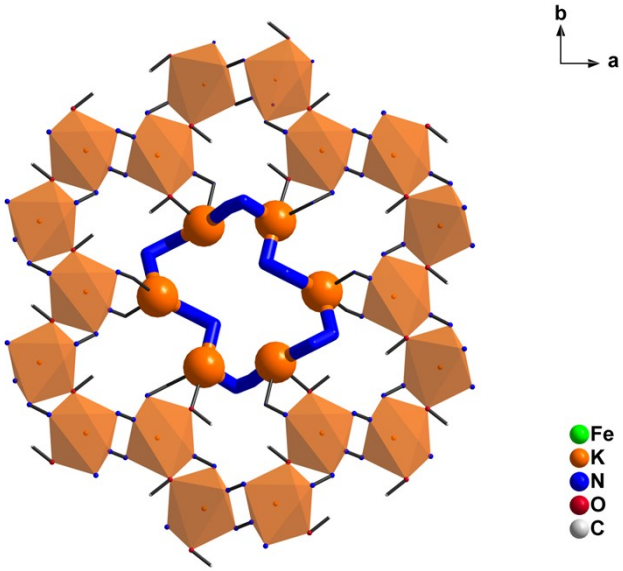

Figure S21. The 18-MC_{K}^{+}-6 like azametallacrown in inorganic layer of compound **2**.

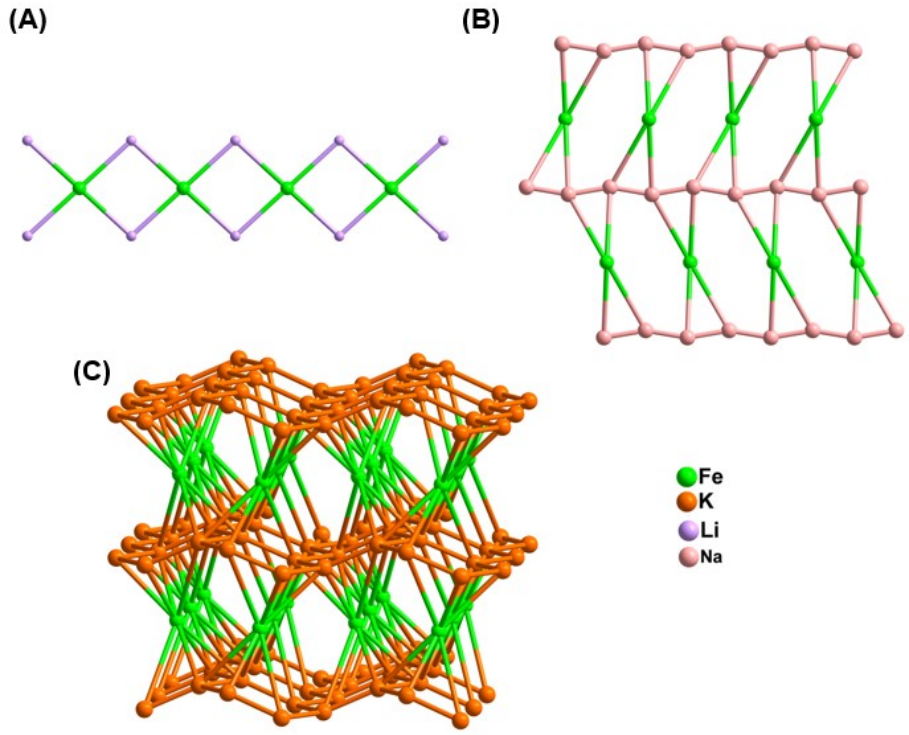

Figure S22. Abstracted topological networks for (A) (2,4)-connected net of **1**, (B) (4, 4)-connected net of **2**, and (C) (7, 8)-connected net of **3**.

5. Solid state magnetic studies

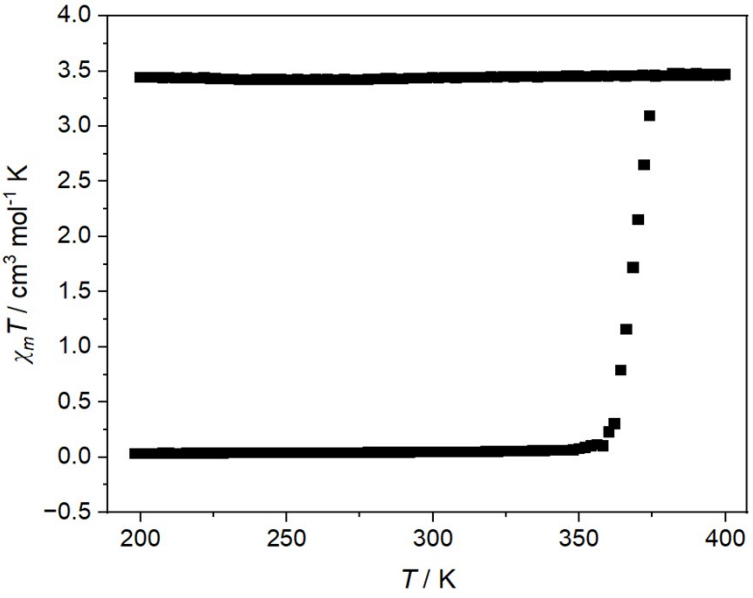

Figure S23. Temperature dependence of the χ_mT product for compound **1** in the temperature range of 2−400 K. Noted: Determining the exact water loss during heating was tricky, so all calculations were based on the molecular weight of the initial formula for compound **1**.

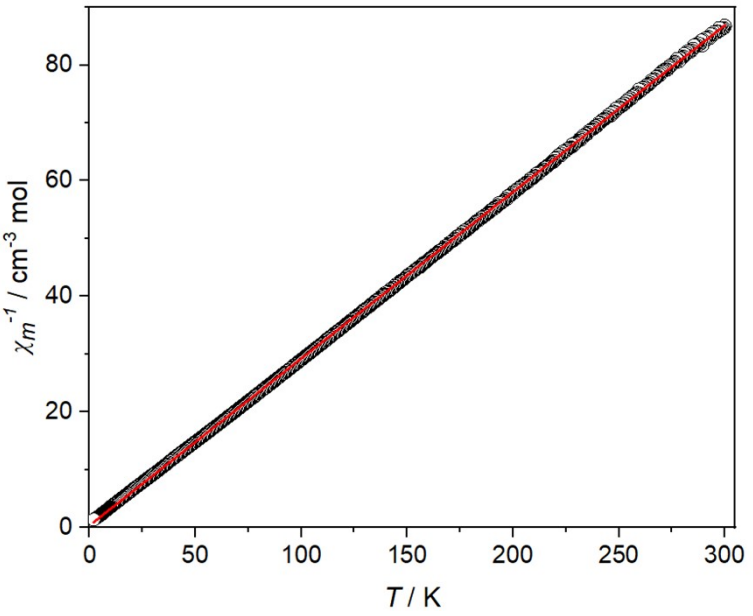

Figure S24. Fitting the magnetic data using the Curie–Weiss equation in the

temperature range 2−300 K, gives a Curie constant of C = 3.47 $cm^3 \cdot K \cdot mol^{-1}$.

6. Solution state magnetic studies

In solution, the ideal solution model was adopted to investigate the SCO properties of compounds **1-3** with the following equation S6, which can be derived by simultaneous Evans Model's equation S1 and ideal Solution Model's equation S2.[5]

$$\chi_M T = \frac{3VM}{4\pi m \times 10^6} * T * \Delta\delta \qquad \textbf{Eq. S1}$$

And

$$\chi_M T = \frac{(\chi_M T)_{HS}}{1 + exp(\frac{\Delta H - T\Delta S}{RT})} \qquad \textbf{Eq. S2}$$

Inserting Eq. S1 into Eq. S2 results in

$$\Delta\delta = \frac{(\chi_M T)_{HS}(\frac{3VM}{4\pi m \times 10^6})^{-1}}{T + Texp(\frac{\Delta H - T\Delta S}{RT})} \qquad \textbf{Eq. S3}$$

Separation constant term C:

$$C = (\chi_M T)_{HS}(\frac{3VM}{4\pi m \times 10^6})^{-1} \qquad \textbf{Eq. S4}$$

$$\Delta\delta = \delta - \delta_{LS} \qquad \textbf{Eq. S5}$$

Inserting Eq. **S4** and Eq. **S5** into Eq. **S3**, it can be written as

$$\delta = \delta_{LS} + \frac{C}{T + Texp(\frac{\Delta H - T\Delta S}{RT})} \qquad \textbf{Eq. S6}$$

δ is the chemical shift of the selected peak; δ_{LS} is the chemical shift of the selected peak on a low spin state of compounds **1**−**3**, which can be replaced by their diamagnetic Zn^{II} analogues. C is a constant; T corresponds to the temperature; ΔH and ΔS correspond to the enthalpy and entropy change of the SCO process and R is the gas constant (8.3145 J mol^{-1} K^{-1}).

Spin state populations were calculated with the thermodynamic parameters

obtained from the fitting results.

$$\gamma_{LS} = \frac{1}{1 + exp(-\frac{\Delta H - T\Delta S}{RT})} \quad \textbf{Eq. S7}$$

$$\gamma_{HS} = 1 - \frac{1}{1 + exp(-\frac{\Delta H - T\Delta S}{RT})} \quad \textbf{Eq. S8}$$

Table S8. Enthalpy ΔH and entropy ΔS during the process of spin crossover and transition temperature ($T_{1/2}$).

Complexes	ΔH (kJ mol^{-1})	ΔS (J mol^{-1} K^{-1})	$T_{1/2}$ (K)
$[FeL_2]^{2-}[Li^+]_2$	24.21	77.89	311
$[FeL_2]^{2-}[Na^+]_2$	25.45	81.43	313
$[FeL_2]^{2-}[K^+]_2$	24.06	77.09	312

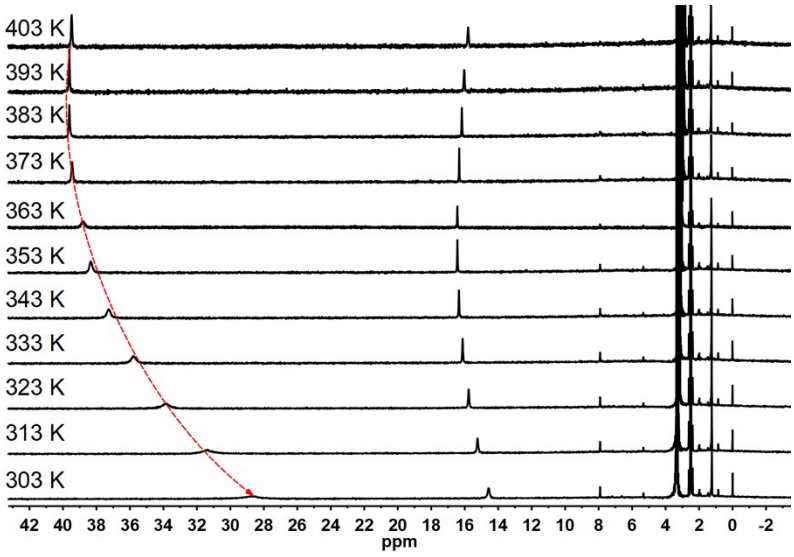

Figure S25. VT ^{1}H-NMR spectra of **1** (600 MHz, d_6-DMSO, from 303 K to 403 K, intervals: 10 K).

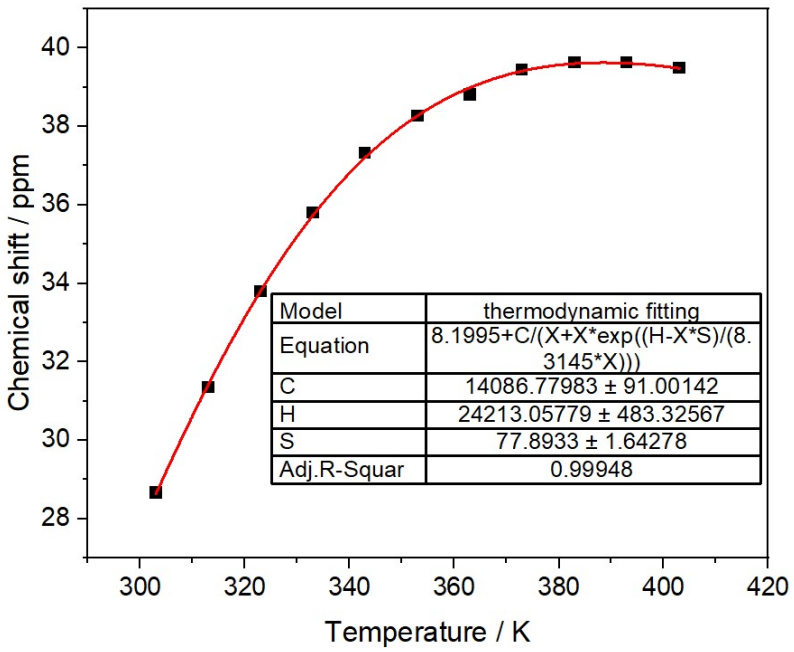

Figure S26. For **1**, ^{1}H NMR chemical shifts of the proton H_b vs temperature, fitting according to **Eq. S6** (600 MHz, d_6-DMSO, from 303 K to 403 K).

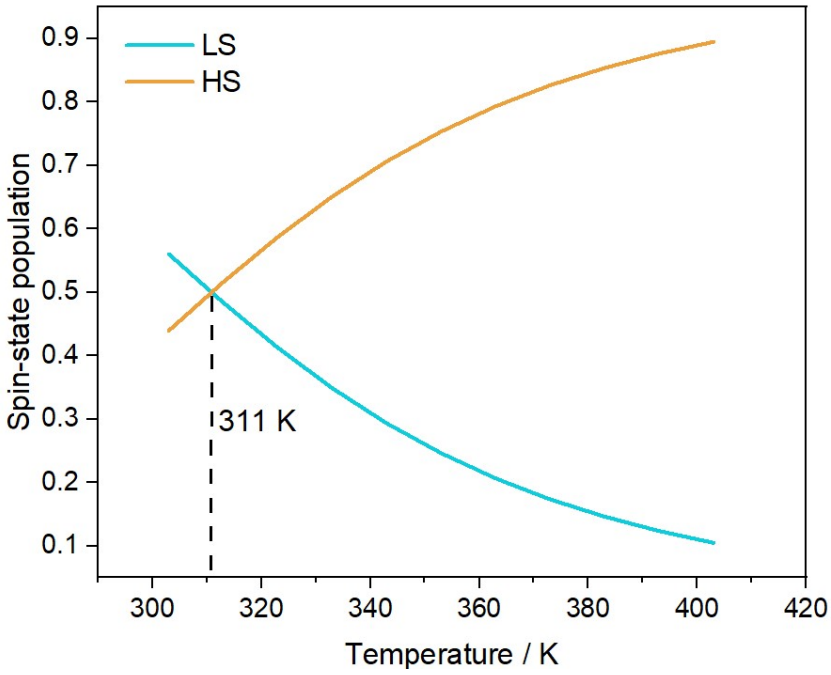

Figure S27. Spin state populations γ of **1** (LS: blue curve, HS: yellow curve) calculated by fitting the data to **Eq. S7 and Eq. S8**.[6] The SCO transition temperature $T_{1/2}$ of 311 K is illustrated with a vertical line.

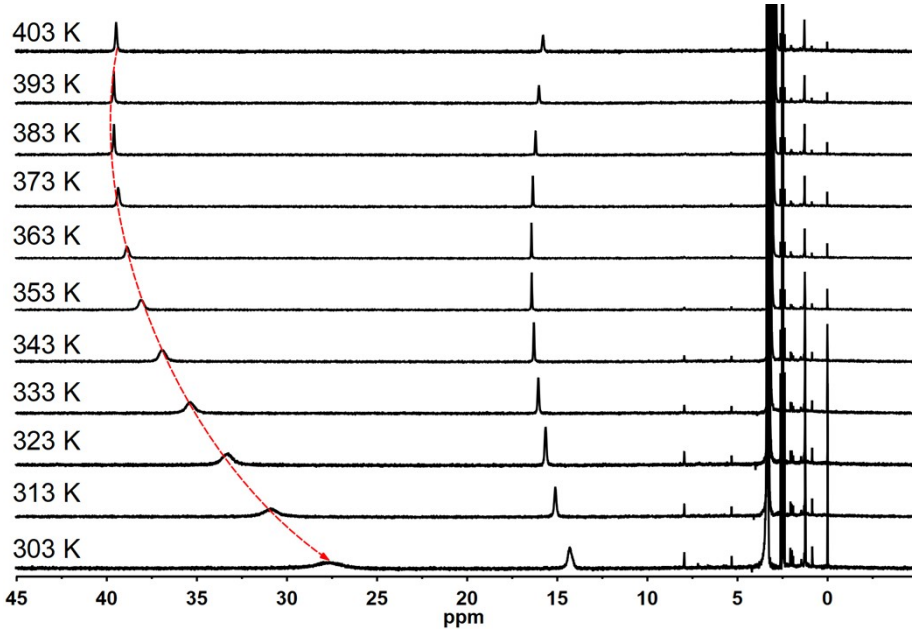

Figure S28. VT ^{1}H-NMR spectra of **2** (600 MHz, d_6-DMSO, from 303 K to 403 K, intervals: 10 K).

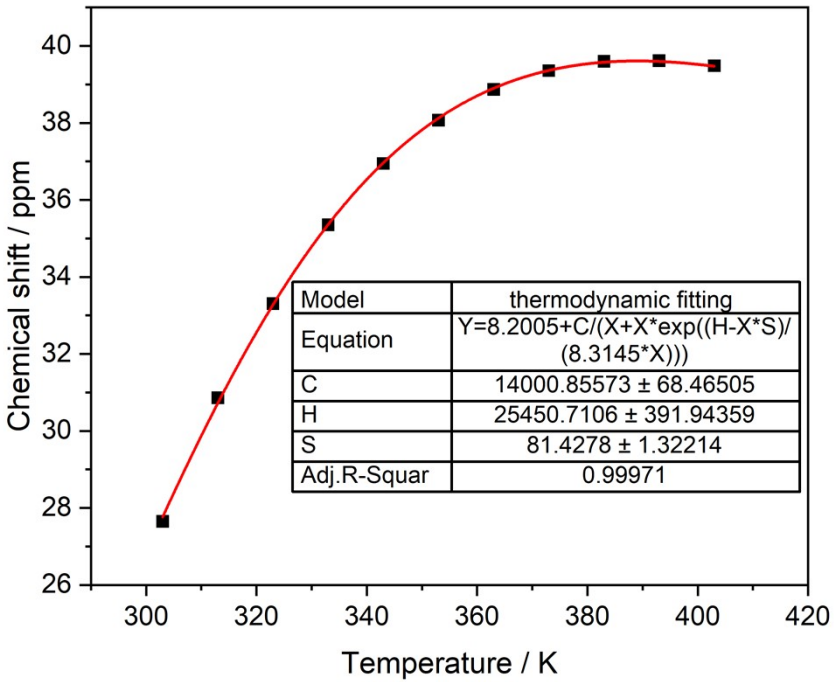

Figure S29. For **2** , ^{1}H NMR chemical shifts of the proton H_b vs temperature, fitting according to Eq. S6 (600 MHz, d_6-DMSO, from 303 K to 403 K).

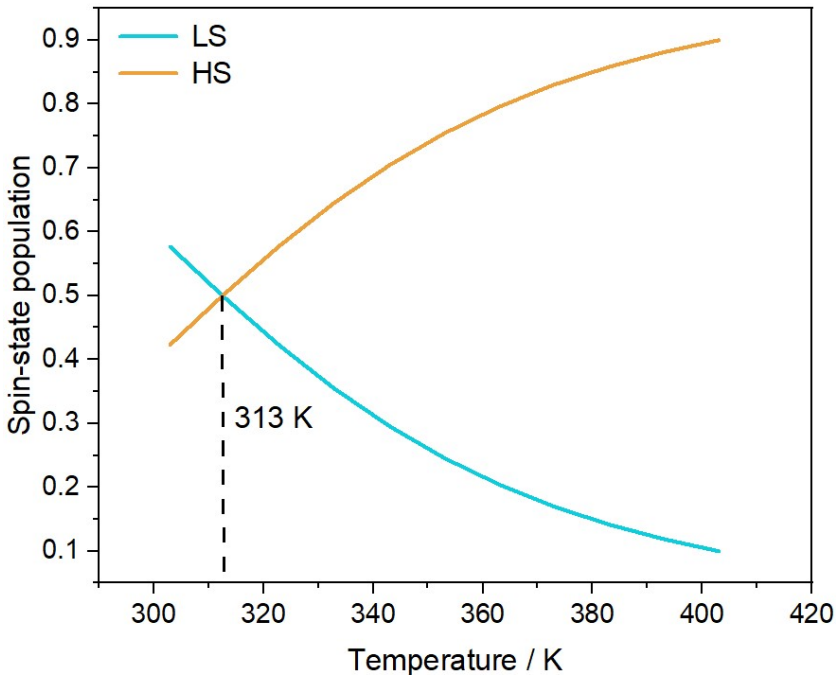

Figure S30. Spin state populations γ of **2** (LS: blue curve, HS: yellow curve) calculated by fitting the data to **Eq. S7 and Eq. S8**. The SCO transition temperature $T_{1/2}$ of 313 K is illustrated with a vertical line.

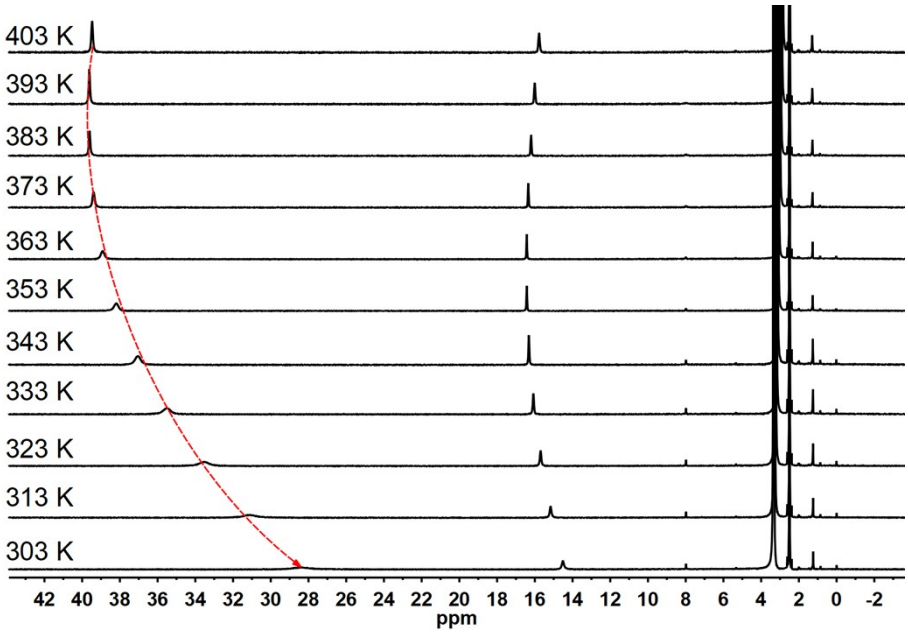

Figure S31. VT ^{1}H-NMR spectra of **3** (600 MHz, d_6-DMSO, from 303 K to 403 K, intervals: 10 K).

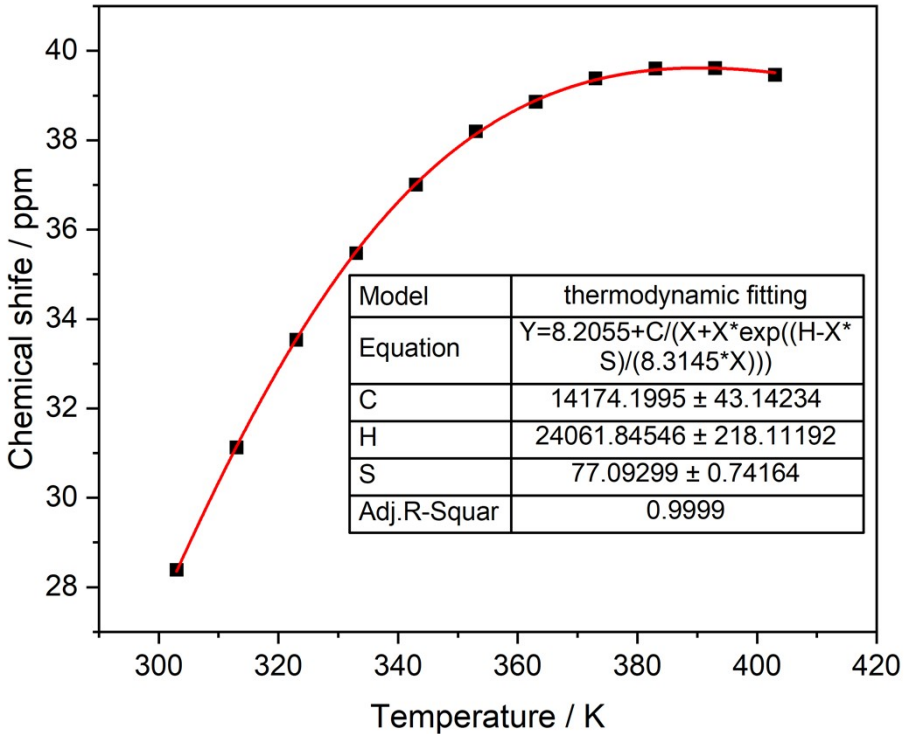

Figure S32. For **3**, ^{1}H NMR chemical shifts of the proton H_b vs temperature, fitting according to **Eq. S6** (600 MHz, d_6-DMSO, from 303 K to 403 K).

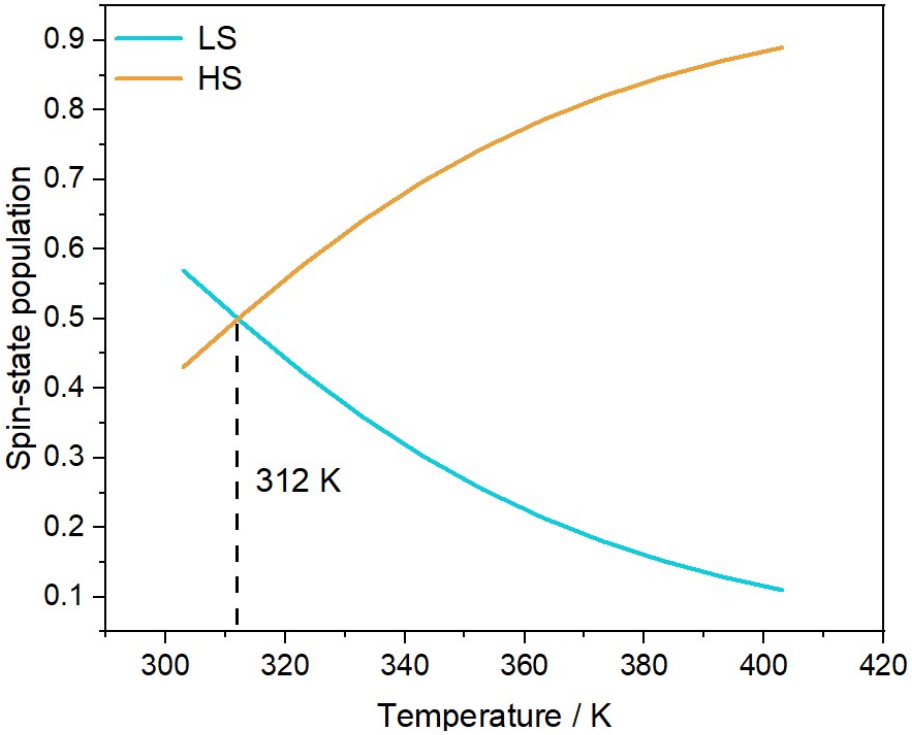

Figure S33. Spin state populations γ of **3** (LS: blue curve, HS: yellow curve) calculated by fitting the data to **Eq. S7 and Eq. S8**. The SCO transition temperature $T_{1/2}$ of 312 K is illustrated with a vertical line.

7. Thermogravimetric analyses (TGA)

To investigate the thermal stability of compounds **1** and **2**, thermogravimetric analyses (TGA) have been performed on powder samples in a N_2 atmosphere at a heating rate of 10 ºC min^{-1}. The TGA curve of **1** indicates that there is a weight loss of 23.11% from 30 to 300 °C, which can be attributed to the loss of eight water molecules (calcd = 22.49%). For **2**, the weight loss occurs over the range of 30−170 °C relevant to the release of six H_2O molecules (obsd = 16.89%, calcd = 16.91%).

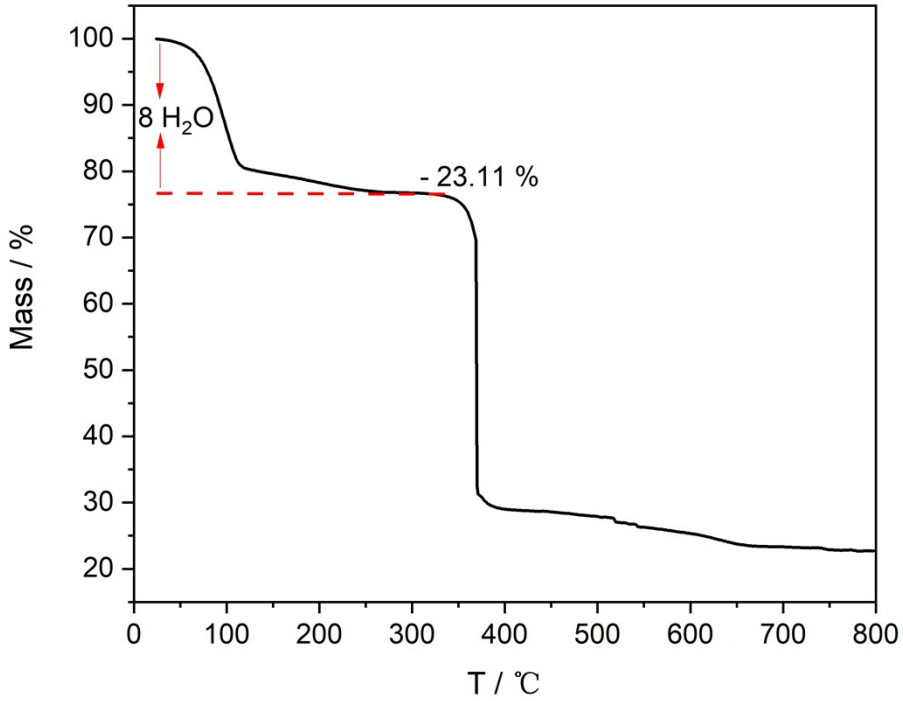

Figure S34. TGA profiles for compound **1**.

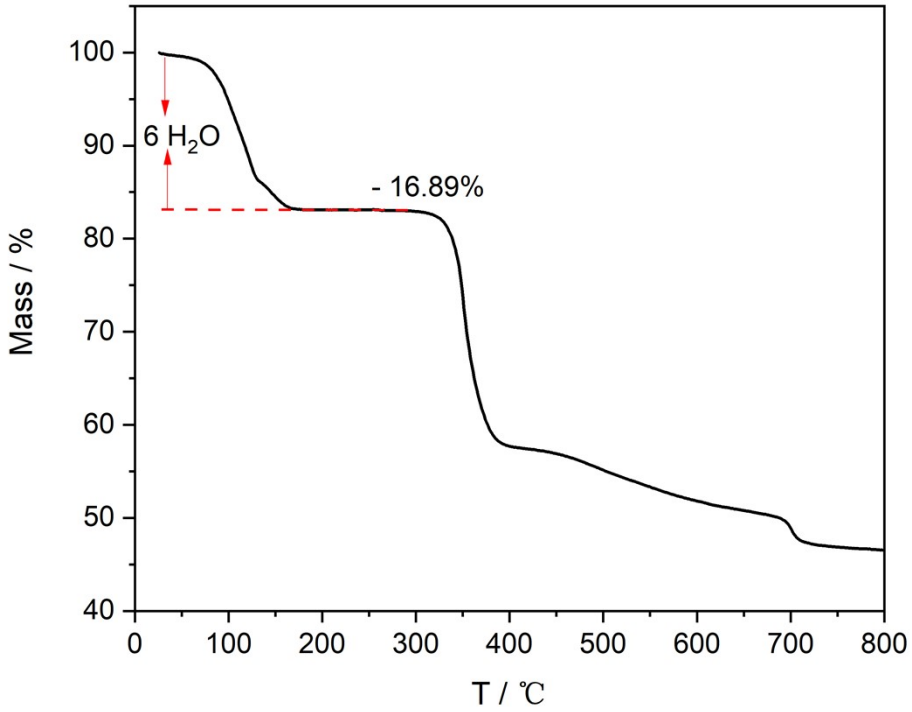

Figure S35. TGA profiles for compound **2**.

8. X-ray Powder diffraction data

The measured PXRD patterns **1–2** match well with the simulated patterns generated from single-crystal X-ray diffraction data, indicating the phase purity of the synthesized crystalline powder sample.

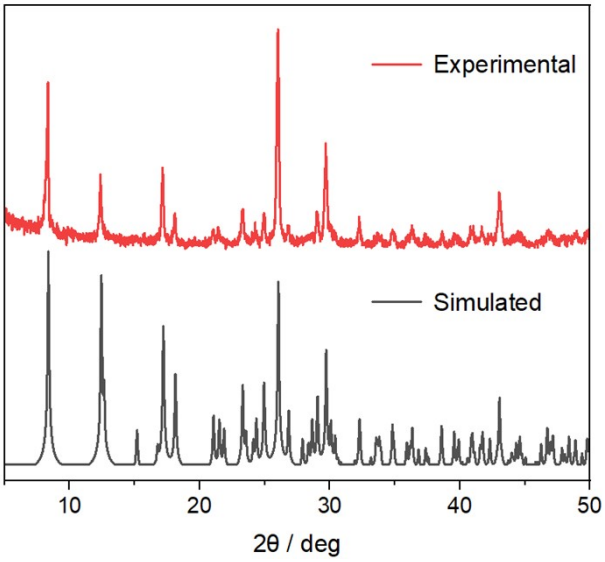

Figure S36. The X-ray powder diffraction data for compound **1**. The simulated data

are obtained from the results of single crystal X-ray diffraction data at 293 K for **1**, respectively.

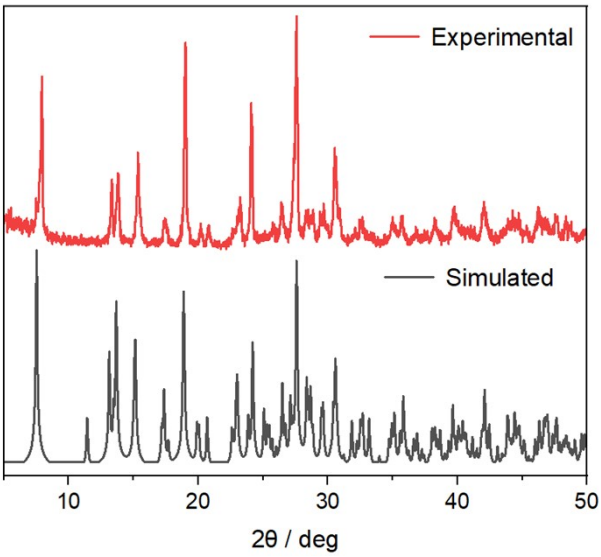

Figure S37. The X-ray powder diffraction data for compound **2**. The simulated data are obtained from the results of single crystal X-ray diffraction data at 100 K,for **2**, respectively.

9. References

1. Liu, J.-H., Guo, X.-Q., Wang, Z.-C., Cai, L.-X., Zhou, L.-P., Tian, C.-B., & Sun, Q.-F. Cation modulated spin state and near room temperature transition within a family of compounds containing the same $[FeL_2]^{2-}$ center. *Dalton Trans*. **2022**. 51, 3894-3901.

2. E. S. Andreiadis, D. Imbert, J. Pecaut, R. Demadrille, M. Mazzanti, Selfassembly of highly luminescent lanthanide complexes promoted by pyridinetetrazolate ligands. Dalton Trans. **2012**, 41, 1268-1277.

3. Agilent Technologies, CrysAlisPro v. 1.171.36.28, **2013**.

4. Dolomanov, O. V., Bourhis, L. J., Gildea, R. J., Howard, J. A. K. and Puschmann, H. "OLEX2: a complete structure solution, refinement and analysis program". *J. Appl. Cryst.* **2009**, 42, 339-341.

5. Yin, F., Yang, J., Zhou, L.-P., Meng, X., Tian, C.-B., & Sun, Q.-F. 54 K Spin Transition Temperature Shift in a Fe6L4 Octahedral Cage Induced by Optimal Fitted Multiple Guests. *J. Am. Chem. Soc.* **2024**, 146, 7811-7821.

6. R. A. Bilbeisi, S. Zarra, H. L. C. Feltham, G. N. L. Jameson, J. K. Clegg, S. Brooker, J. R. Nitschke, *Chem. Eur. J.* **2013**, 19, 8058 – 8062.